7-8-2024

Contributions of Brain Microstructures and Metabolism to Visual Field Loss Patterns in Glaucoma Using Archetypal and Information Gain Analyses

Yueyin Pang

Ji Won Bang

Anisha Kasi

Jeremy Li

Carlos Parra

See next page for additional authors

Authors

Yueyin Pang, Ji Won Bang, Anisha Kasi, Jeremy Li, Carlos Parra, Els Fieremans, Gadi Wollstein, Joel S. Schuman, Mengyu Wang, and Kevin C Chan

Contributions of Brain Microstructures and Metabolism to Visual Field Loss Patterns in Glaucoma Using Archetypal and Information Gain Analyses

Yueyin Pang,[1] Ji Won Bang,[1] Anisha Kasi,[1] Jeremy Li,[1] Carlos Parra,[1] Els Fieremans,[2,3] Gadi Wollstein,[1,3–6] Joel S. Schuman,[5–7] Mengyu Wang,[8] and Kevin C. Chan[1–4,9]

[1]Department of Ophthalmology, New York University Grossman School of Medicine, New York, New York, United States
[2]Department of Radiology, New York University Grossman School of Medicine, New York, New York, United States
[3]Department of Biomedical Engineering, Tandon School of Engineering, New York University, Brooklyn, New York, United States
[4]Center for Neural Science, New York University, New York, New York, United States
[5]Wills Eye Hospital, Philadelphia, Pennsylvania, United States
[6]Sidney Kimmel Medical College, Thomas Jefferson University, Philadelphia, Pennsylvania, United States
[7]Drexel University School of Biomedical Engineering, Science and Health Studies, Philadelphia, Pennsylvania, United States
[8]Schepens Eye Research Institute, Harvard Medical School, Boston, Massachusetts, United States
[9]Neuroscience Institute and Tech4Health Institute, New York University Grossman School of Medicine, New York, New York, United States

PURPOSE. To investigate the contributions of the microstructural and metabolic brain environment to glaucoma and their association with visual field (VF) loss patterns by using advanced diffusion magnetic resonance imaging (dMRI), proton magnetic resonance spectroscopy (MRS), and clinical ophthalmic measures.

METHODS. Sixty-nine glaucoma and healthy subjects underwent dMRI and/or MRS at 3 Tesla. Ophthalmic data were collected from VF perimetry and optical coherence tomography. dMRI parameters of microstructural integrity in the optic radiation and MRS-derived neurochemical levels in the visual cortex were compared among early glaucoma, advanced glaucoma, and healthy controls. Multivariate regression was used to correlate neuroimaging metrics with 16 archetypal VF loss patterns. We also ranked neuroimaging, ophthalmic, and demographic attributes in terms of their information gain to determine their importance to glaucoma.

RESULTS. In dMRI, decreasing fractional anisotropy, radial kurtosis, and tortuosity and increasing radial diffusivity correlated with greater overall VF loss bilaterally. Regionally, decreasing intra-axonal space and extra-axonal space diffusivities correlated with greater VF loss in the superior–altitudinal area of the right eye and the inferior–altitudinal area of the left eye. In MRS, both early and advanced glaucoma patients had lower gamma-aminobutyric acid (GABA), glutamate, and choline levels than healthy controls. GABA appeared to associate more with superonasal VF loss, and glutamate and choline more with inferior VF loss. Choline ranked third for importance to early glaucoma, whereas radial kurtosis and GABA ranked fourth and fifth for advanced glaucoma.

CONCLUSIONS. Our findings highlight the importance of non-invasive neuroimaging biomarkers and analytical modeling for unveiling glaucomatous neurodegeneration and how they reflect complementary VF loss patterns.

Keywords: brain, diffusion magnetic resonance imaging, glaucoma, optic radiation, proton magnetic resonance spectroscopy, visual cortex, visual field

G laucoma refers to a group of age-related optic neuropathies and is the leading cause of irreversible blindness, impacting more than 70 million people globally.[1] The most common type is primary open-angle glaucoma, which involves slow and characteristic damage to the optic nerve and loss of retinal ganglion cells along with progressive vision loss.[2] Intraocular pressure is currently the only clinically modifiable risk factor for glaucoma.[3] However, around 20% of patients with glaucoma have normal intraoc-ular pressure, but nearly 90% of people with high intraocular pressure do not get glaucoma.[4] This indicates that, although elevated eye pressure is an important risk factor, it alone cannot account for all aspects of disease onset and progression. The exact causes of glaucoma are not fully understood but likely involve multiple factors such as age, genetics, cerebrovasculature, neuroinflammation, and diabetes.[5–7,67–69] Current treatments for glaucoma only target lowering intraocular pressure but unfortunately do not

directly protect the optic nerve.[8] As damage to the central nervous system remains unrecoverable, vision loss from glaucomatous damage to the visual pathway is currently irreversible. Thus, early detection of glaucoma is necessary to prevent vision loss but is quite challenging due to its insidious onset and asymptomatic nature in the early stages. Further research into disease mechanisms and improved detection techniques are necessary in order to identify early biomarkers to enable timely intervention, prevent vision loss and blindness, and reduce the ongoing major public health burden of glaucoma globally.[9,10]

Recent neuroimaging research using magnetic resonance imaging (MRI) and magnetic resonance spectroscopy (MRS) has identified brain abnormalities in the visual pathways related to glaucoma damage.[11–18] MRI utilizes strong magnetic fields and radio waves to generate detailed three-dimensional structural, physiological, and functional images of the brain and other tissues, whereas MRS measures metabolites, such as gamma-aminobutyric acid (GABA), creatine, choline, and glutamate, that play key roles in neuronal health and function. Specific MRI techniques such as voxel-based morphometry, cortical thickness mapping, and diffusion tensor imaging can detect subtle structural changes in gray and white matter regions related to glaucoma.[19–22] For example, diffusion-based MRI is sensitive to microstructural alterations in white matter tracts and has revealed decreased optic radiation integrity in glaucoma patients,[23] whereas recent MRS studies have revealed metabolic alterations in the visual cortex associated with glaucoma.[24,25] Taken together, these findings support the presence of trans-synaptic neurodegeneration in glaucoma.[26] However, the link between structural or metabolic neurodegenerative changes in brain MRI/MRS and vision loss in glaucoma is not fully characterized. Elucidating the connections between imaging biomarkers and visual function in glaucoma will advance our understanding of disease mechanisms, allow improved tracking of severity, and facilitate evaluation of neuroprotective therapies beyond targeting intraocular pressure alone. This study aimed to investigate how structural and metabolic brain changes may contribute to visual field defects in glaucoma patients. Determining such structural, metabolic, and functional relationships will provide insight into the extent of neurodegeneration in the visual pathway that accompanies glaucomatous vision loss.

METHODS

Subject Recruitment

This study was approved by the Institutional Review Board of New York University Grossman School of Medicine and followed the tenets of the Declaration of Helsinki. Informed consent was obtained from all participants. Twenty early glaucoma, 28 advanced glaucoma, and 21 healthy subjects were recruited from the Department of Ophthalmology at New York University Grossman School of Medicine. All subjects had best-corrected visual acuity of 20/60 or better and no history or evidence of retinal or neurological disorders other than glaucoma. Glaucoma subjects had clinically diagnosed primary glaucoma, and the healthy controls had no glaucomatous conditions. Exclusion criteria included pregnancy, breastfeeding, metal implants besides dental fillings, anxiety, claustrophobia, and obesity preventing MRI scanner placement.

Clinical Ophthalmic Examinations

Clinical ophthalmic assessments were performed on both glaucoma patients and healthy subjects, which included peripapillary retinal nerve fiber layer (pRNFL) thickness and optic nerve head cup-to-disc ratio, using a CIRRUS spectral-domain optical coherence tomography device (Carl Zeiss Meditec, Dublin, CA, USA) and visual field mean deviation (VF-MD) based on the Swedish interactive thresholding algorithm (SITA) 24-2 standard test (Humphrey Field Analyzer; Carl Zeiss Meditec). The average VF-MD of both eyes was used to categorize patients into early or advanced glaucoma groups. Early glaucoma was defined as patients with average VF-MD better than –6.0 dB, and advanced glaucoma was defined as those with average VF-MD worse than –6.0 dB following previous literature.[27,28] The pointwise total deviations of 24-2 visual field tests were also collected from the Humphrey visual field perimetry for partial correlations with diffusion MRI and MRS parameters followed by visual field pattern analysis.[29] In a prior landmark study, 16 representative 24-2 visual field patterns, or archetypes (ATs), were determined by an unsupervised machine learning method termed archetypal analysis, which determines patterns on the corners of the data space resembling extreme cases observed.[30] The 16 visual field archetypal patterns are consistent with visual field patterns clinically summarized[31] (Fig. 1). In more recent studies, archetypal analysis was applied to detect visual field progression, identify false-positive glaucomatous visual fields,[32,33] and quantify central visual field loss patterns from the Humphrey 10-2 SITA Standard protocol.[34,35]

MRI Protocol

All healthy and glaucoma subjects underwent brain MRI scanning using a Siemens MAGNETOM Prisma 3-Tesla scanner (Siemens, Munich, Germany) equipped with a 20-channel head/neck coil at the NYU Langone Health Center for Biomedical Imaging. High-resolution T1-weighted anatomical images were first acquired covering the whole brain using a multi-echo magnetization-prepared rapid gradient echo (MPRAGE) sequence, with 256 slices, voxel size = $0.8 \times 0.8 \times 0.8$ mm^3, repetition time = 2400 ms, echo time = 2.24 ms, flip angle = 8°, field of view = 256×256 mm^2, and bandwidth = 210 Hz per pixel. Diffusion-weighted MRI was performed at multiple shells comprised of three diffusion weighting factors (*b* values) at 250, 1000, and 2000 s/mm^2, along with multiple diffusion encoding directions of 4, 20, and 60, respectively, using echo-planar imaging. Ten non-diffusion weighted images at $b = 0$ s/mm^2 were also acquired. Other imaging parameters included field of view = 230×230 mm^2, acquisition matrix = 100×100, voxel resolution = $2.3 \times 2.3 \times 2.3$ mm^3, number of slices = 52, repetition time = 5000 ms, and echo time = 70 ms. Total acquisition time was about 10 minutes. For proton MRS, a $2.2 \times 2.2 \times 2.2$-cm^3 voxel was manually positioned along the calcarine sulcus to cover the visual cortex of both hemispheres. Upon automated shimming, GABA concentration was measured using the Mescher–Garwood point-resolved spectroscopy sequence with double-banded pulses, with repetition time = 1500 ms, echo time = 68 ms, 172 averages, and 522-second duration. The GABA-edited spectrum was obtained by subtracting the edit-off spectrum from the edit-on spectrum. Glutamate and choline were measured from the same voxel using the
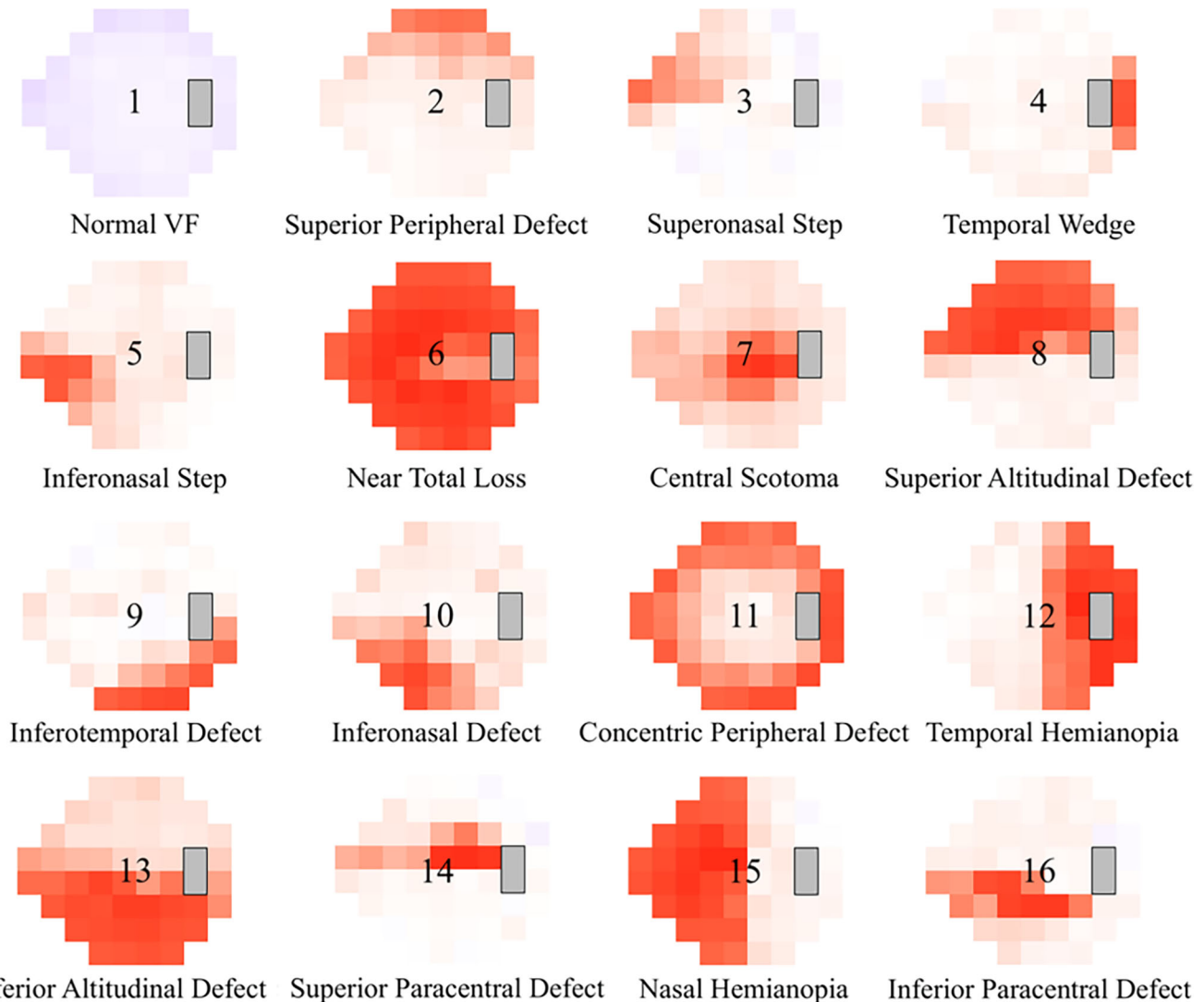
FIGURE 1. Glaucoma visual field loss archetypes. Sixteen pre-established glaucoma visual field loss archetypes are presented, including the normal visual field archetype (AT1). Adapted from Elze et al.[30]

point-resolved spectroscopy (PRESS) sequence with repetition time = 3000 ms, echo time = 30 ms, 99 averages, and 300-second duration. We used anatomical landmarks based on T1-weighted MRI and the human brain atlas to ensure consistent localization of diffusion MRI and proton MRS measurements across subjects. During MRS scans, subjects performed a fixation task to maintain attention and alertness. A fixation point was presented centrally against a gray background. Subjects were instructed to fixate on this point. The fixation point unpredictably changed color from white to red and back to white after 1.5 seconds. Subjects were to press a button within 1.5 seconds of the color change, which was recorded as a hit. Missed responses were recorded as misses. There was no significant difference in accuracy between healthy controls and early or advanced glaucoma patients ($P > 0.05$).

Diffusion MRI Data Processing and Archetypal Analyses

The preprocessing steps for the diffusion images included eddy current distortion and motion correction in FSL 5.0.10,

as well as Marchenko–Pastur principal component analysis denoising, Gibbs ringing correction, Rician bias correction, outlier detection, and smoothing using the Diffusion parameter EStimation with Gibbs and NoisE Removal (DESIGNER) suite.[36] We then used DESIGNER to calculate maps of diffusion tensor imaging (DTI), including fractional anisotropy, axial diffusivity, radial diffusivity, and mean diffusivity; diffusion kurtosis imaging (DKI), including mean kurtosis, axial kurtosis, and radial kurtosis; and the DKI-extended white matter tract integrity (WMTI) parameters of intra-axonal space axial diffusivity, axial extra-axonal space diffusivity (EASD parallel), radial EAS diffusivity (EASD perpendicular), axonal water fraction, and tortuosity of the EAS (ratio of EASD parallel and EASD perpendicular).[17,36,37] All maps were nonlinearly registered to the FMRIB58 fractional anisotropy standard-space image in FSL. Regions of interest were delineated on the left and right optic radiations of the fractional anisotropy map using the brain atlas. The same regions of interest were then applied to other parametric maps. The mean values of DTI, DKI, and WMTI parameters were estimated for the averaged left and right hemispheres. These parameters were compared between

groups using analysis of variance (ANOVA) and post hoc Tukey's tests. Partial correlation analyses were used to associate diffusion MRI parameters with regional visual field loss measured by pointwise total deviation values. Sixteen previously established visual field loss archetypes[30] were used to analyze the associations between diffusion MRI parameters and visual field loss patterns in specific areas using multivariate linear regression (Fig. 1). Results were considered statistically significant for $P < 0.05$.

MRS Data Processing and Archetypal Analyses

GABA, glutamate, choline, and creatine levels were quantified from the spectra using LCModel.[38] We normalized the concentrations of GABA, glutamate, and choline using the amount of total creatine, which is commonly used as a standard reference resonance to account for systematic fluctuations between experimental sessions.[38,39] These normalized metabolites were then compared between groups using ANOVA and post hoc Tukey's tests. Partial correlations analyses were performed to associate metabolites levels with total deviations of 24-2 visual field tests. The resulting visual field models were aligned with the 16 predefined archetypal patterns of visual field loss[30] using multivariate linear regression. Results were considered statistically significant for $P < 0.05$.

Information Gain and Multilayer Perceptron Analyses

It is currently unclear how important structural and metabolic brain changes are to the pathogenesis of glaucoma. With the growing development of artificial intelligence methods in biomedical research, recent studies have utilized feature selection techniques in machine learning to rank the importance of contributing factors to disease, namely through information gain.[40–43] Information gain is a metric that measures the contribution of a feature to the reduction in entropy of a dataset. The Weka (University of Waikato, Auckland, New Zealand) attribute evaluator InfoGainAttributeEval measures the information gain of an attribute with respect to the class, calculating a numerical "worth" of each attribute in a dataset.[44] "Worth" is a numerical representation of how important a given attribute is in discriminating between the classes. In our dataset, our classes were healthy controls, early glaucoma, and advanced glaucoma. Each of the attributes was fed into the InfoGain evaluator, which assigned each attribute a worth and ranked the attributes in descending order of worth. In this study, we sought to use InfoGain with 10-fold cross-validations in the Weka software to rank all descriptors in terms of their information gain in distinguishing between healthy controls and early or advanced glaucoma. We assessed the information gain for each of the following 21 attributes: age, gender, race, VF-MD, pRNFL thickness, cup-to-disc ratio, 12 diffusion MRI measures of the optic radiation, and three MRS metabolite levels in the visual cortex.

We also ran the machine learning algorithm multilayer perceptron (MLP) to determine the accuracy and area under the receiver operating characteristics (ROC) curve. We ran the MLP algorithm twice, first with the full list of 21 attributes and then with a reduced list of attributes, which included only those with an attribute worth >0 in the InfoGain ranking analysis. The accuracy of this model was calculated based on the percentage of total instances in which the model correctly classified glaucoma severity. The ROC area is a measure of how efficient the MLP model is, which is calculated by plotting the true-positive rate against the false-positive rate and calculating the area under the curve.

RESULTS

All 69 subjects underwent diffusion MRI and proton MRS using the 3-Tesla MRI scanner. Among these subjects, diffusion MRI data from seven early glaucoma subjects and MRS data from two healthy subjects were not included in the analyses due to technical issues. Tables 1 and 2 provide demo-

TABLE 1. Demographics and Clinical Ophthalmic Measures for Diffusion MRI Analyses

Demographic	Healthy ($n = 21$)	Early Glaucoma ($n = 13$)	Advanced Glaucoma ($n = 28$)	Significance H vs. EG, EG vs. AG, H vs. AG
Age (y), mean ± SD	63.74 ± 1.65	68.49 ± 1.85	65.60 ± 1.36	ns, ns, ns
Sex, female/male, n	14/7	9/4	14/14	ns, ns, ns
Race, n				
White	14	9	15	ns, ns, ns
African American	2	2	6	ns, ns, ns
Asian	3	0	3	ns, ns, ns
Other race	2	2	4	ns, ns, ns
pRNFL thickness (µm), mean ± SD				
OD	89.61 ± 8.02	72.14 ± 12.58	61.54 ± 9.58	**, **, *
OS	78.12 ± 8.19	68.01 ± 7.24	60.21 ± 8.20	*, ns, **
Optic nerve head C/D, mean ± SD				
OD	0.45 ± 0.15	0.67 ± 0.19	0.65 ± 0.11	**, ns, **
OS	0.42 ± 0.15	0.64 ± 0.18	0.73 ± 0.11	**, **, *
Visual field mean deviation (dB), mean ± SD				
OD	−2.32 ± 4.32	−1.58 ± 2.29	−17.7 ± 1.67	ns, **, **
OS	−1.41 ± 1.67	−2.00 ± 2.51	−13.48 ± 1.81	ns, **, **

This table compares demographic and clinical ophthalmic measures among the three groups that were included for diffusion MRI analyses. Statistical tests including one-way ANOVA and Tukey's post hoc analysis or χ^2 tests were used to evaluate between-group differences. H, healthy controls; EG, early glaucoma; AG, advanced glaucoma; OD, oculus dexter (right eye); OS, oculus sinister (left eye); C/D, cup-to-disc ratio; ns, not significant.

* $P < 0.05$.
** $P < 0.01$.

TABLE 2. Demographics and Clinical Ophthalmic Measures for Proton MRS Analyses

Demographic	Healthy ($n = 19$)	Early Glaucoma ($n = 20$)	Advanced Glaucoma ($n = 28$)	Significance H vs. EG, EG vs. AG, H vs. AG
Age (y), mean ± SD	63.68 ± 1.91	66.75 ± 1.60	65.60 ± 1.36	ns, ns, ns
Sex, F/M, *n*	12/7	13/7	14/14	ns, ns, ns
Race, *n*				
White	14	12	15	ns, ns, ns
African American	0	3	6	ns, ns, ns
Asian	3	1	3	ns, ns, ns
Other race	2	4	4	ns, ns, ns
Average pRNFL thickness (µm), mean ± SD				
OD	86.12 ± 2.13	71.19 ± 3.07	61.54 ± 9.58	**,**,*
OS	79.32 ± 6.31	69.21 ± 6.30	60.21 ± 8.20	*,**,*
Optic nerve head C/D, mean ± SD				
OD	0.55 ± 0.19	0.60 ± 0.15	0.65 ± 0.11	ns, **,**
OS	0.41 ± 0.12	0.62 ± 0.18	0.73 ± 0.11	**,**,*
Visual field mean deviation (dB), mean ± SD				
OD	−2.38 ± 1.11	−1.74 ± 0.65	−17.7 ± 1.67	ns, **,**
OS	−1.45 ± 0.45	−2.35 ± 0.65	−13.48 ± 1.81	ns, **,**

This table compares demographic and clinical ophthalmic measures among the three groups that were included for MRS analyses. Statistical tests including one-way ANOVA and Tukey's post hoc analysis or χ^2 tests were used to evaluate between-group differences.
* $P < 0.05$.
** $P < 0.01$.

graphic and clinical information for the analyzed subjects in each modality. Clinical ophthalmic measurements were significantly different among the groups, whereas age, sex, and race were not significantly different. In diffusion MRI, decreasing fractional anisotropy in diffusion tensor imaging, decreasing radial kurtosis in diffusion kurtosis imaging, and decreasing tortuosity in the white matter tract integrity model correlated generally with worse overall visual field loss in both eyes (Fig. 2). In MRS, lower GABA, glutamate, and choline levels were found in early and advanced glaucoma patients compared to healthy subjects (Fig. 3).

In the archetypal analyses between diffusion MRI and visual field loss patterns, increasing fractional anisotropy, radial kurtosis, axonal water fraction, intra-axonal space axial diffusivity, tortuosity, and EASD parallel showed a positive coefficient to the normal visual field archetype (AT1). Increasing fractional anisotropy, radial kurtosis, axonal water fraction, and tortuosity also had a negative coefficient to the overall visual field loss archetype (AT6), whereas increasing radial diffusivity and EASD perpendicular had a positive coefficient to the overall visual field loss archetype (AT6) (Tables 3–5). Regionally, increasing radial diffusivity was associated with concentric peripheral defect (AT11) in the left eye and marginally with central scotoma in the right eye (AT7). Decreasing fractional anisotropy was associated with inferior altitudinal defect (AT13) in the left eye and with central scotoma (AT7) and superior altitudinal defect (AT8) marginally in the right eye. Decreasing radial kurtosis was associated with central scotoma (AT7) in the right eye. Decreasing intra-axonal space axial diffusivity was associated with superior altitudinal defect (AT8) and nasal defect (AT15) in the right eye and with inferior altitudinal defect (AT13) in the left eye. Decreasing tortuosity was associated with superior altitudinal defect (AT8) in the right eye and inferior altitudinal defect (AT13) in the left eye. Decreasing EASD parallel was associated with superior altitudinal defect (AT8) and nasal defect (AT15) in the right eye and with inferior altitudinal defect (AT13) in the left eye. EASD perpendicular

was associated with inferonasal defect (AT10) in left eye (Tables 3–5).

In the archetypal analyses between MRS and visual field loss patterns, increasing GABA, glutamate and choline levels were positively associated with the normal visual field archetype (AT1), whereas decreasing GABA and glutamate levels were marginally associated with worse overall visual field loss archetype (AT6) (Table 6). Regionally, decreasing GABA was associated with worse nasal defect (AT15) in the right eye and marginally with greater visual field loss in the superonasal step area (AT3) in the left eye, whereas decreasing glutamate was marginally associated with greater visual field loss in the inferior altitudinal (AT13) area in the left eye. Decreasing choline was associated with greater visual field loss in the inferonasal (AT10) area in the right eye. Taken together, these neurometabolites appeared to associate with complementary regional patterns of visual field loss in glaucoma, with GABA affecting the superonasal areas more and glutamate and choline affecting the inferior areas more.

The information gain analysis yielded five attributes that had an attribute worth >0 for the comparison between healthy controls and early glaucoma. The corresponding ranking was as follows: (1) pRNFL thickness, (2) cup-to-disc ratio, (3) choline, (4) race, and (5) gender (Fig. 4). For the comparison between healthy controls and advanced glaucoma, the information gain analysis yielded nine attributes that had an attribute worth >0. The corresponding ranking was as follows: (1) VF-MD, (2) pRNFL thickness, (3) cup-to-disc ratio, (4) radial kurtosis, (5) GABA, (6) intra-axonal space axial diffusivity, (7) tortuosity, (8) race, and (9) gender (Fig. 4). Inclusive of all of the attributes regardless of their information gain, MLP was able to differentiate between healthy control and early glaucoma (accuracy, 84.8%; ROC, 0.946) and between healthy control and advanced glaucoma (accuracy, 95.74%; ROC, 0.996). When MLP was performed on the reduced list of attributes that had an information gain attribute worth >0, we saw an improved ability to differentiate between healthy control and
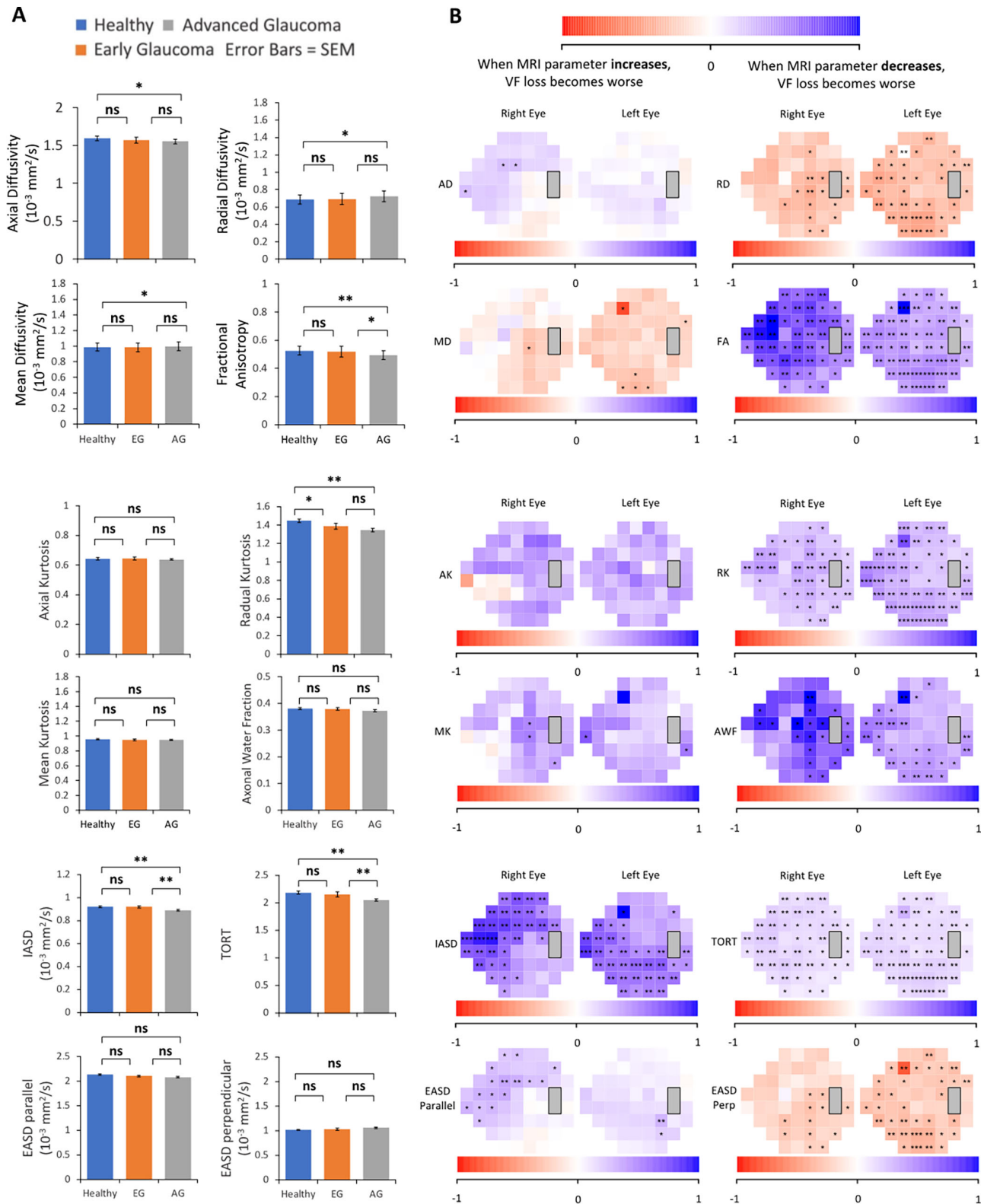
Figure 2. Diffusion MRI parameters and their associations with VF function in glaucoma patients and healthy controls. (**A**) ANOVA and Tukey's post hoc tests were used for between-group comparisons. *Brackets* indicate the significance of differences between subject group pairs: heathy (H) versus early glaucoma (EG), EG versus advanced glaucoma (AG), and H versus AG. (**B**) Partial correlations were performed to show how diffusion MRI parameters were associated to the 52 points in the 24-2 VF across all subjects. *Blue* indicates decreases in the diffusion MRI parameter and VF total deviation (i.e., worse VF loss/positive correlation), and vice versa for *red*. Tortuosity of the EAS is the ratio of EASD parallel to EASD perp. *$P < 0.05$, **$P < 0.01$; AD, axial diffusivity; AK, axial kurtosis; AWF, axonal water fraction; EAS, extra-axonal space; EASD, extra-axonal space diffusivity; EASD parallel, axial EASD; EASD perp, radial EASD; FA, fractional anisotropy; IASD, intra-axonal space axial diffusivity; MD, mean diffusivity; MK, mean kurtosis; ns, not significant; RD, radial diffusivity; RK, radial kurtosis.
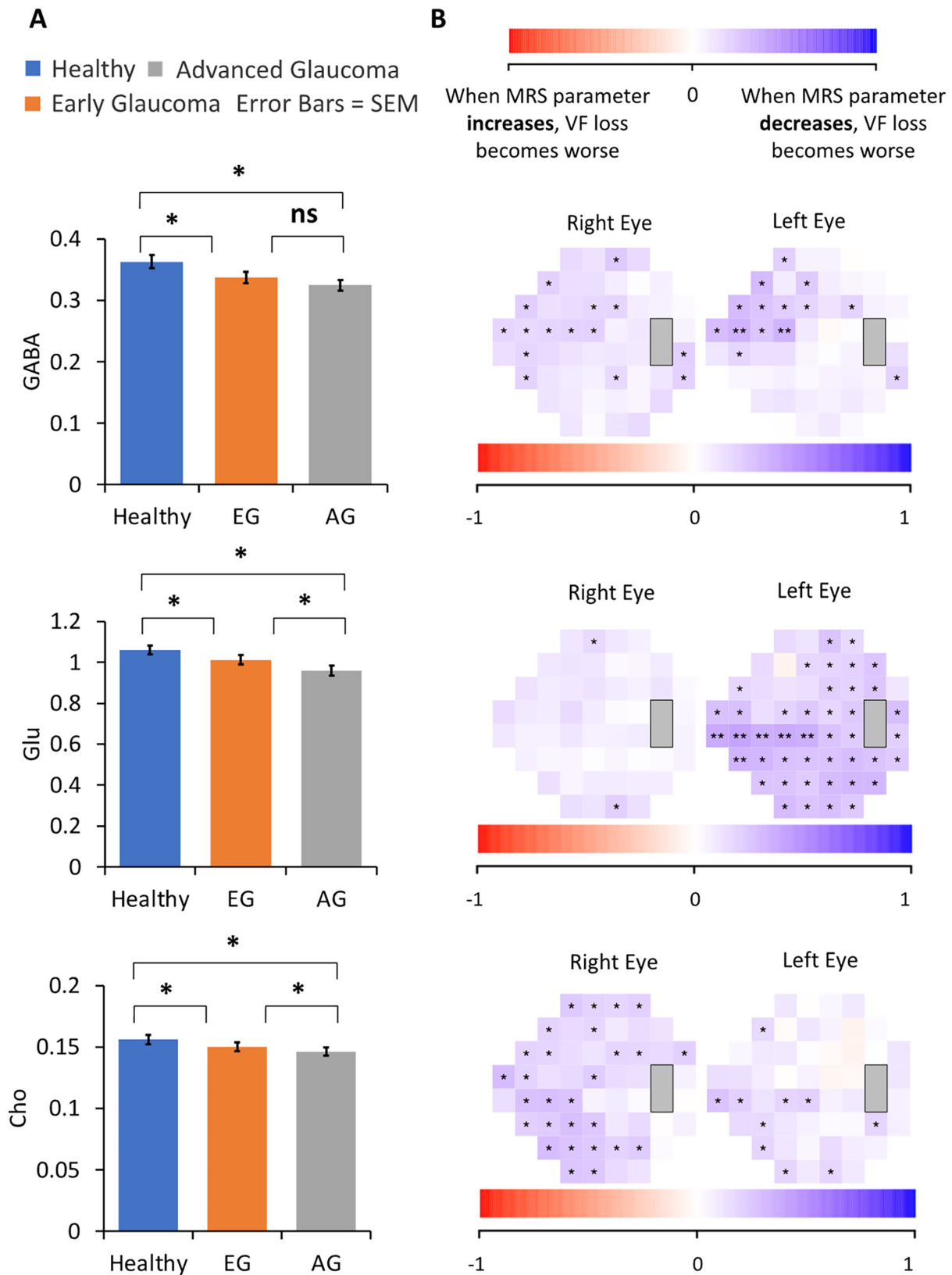
FIGURE 3. GABA, glutamate (Glu), and choline (Cho) levels and their associations with VF function in glaucoma patients and healthy controls. (**A**) ANOVA and Tukey's post hoc tests were used for between-group comparisons. *Brackets* indicate the significance of differences between subject group pairs: heathy (H) versus early glaucoma (EG), EG versus advanced glaucoma (AG), and H versus AG. (**B**) Partial correlations were performed to show how MRS parameters were associated with the 52 points in the 24-2 VF across all subjects. *Blue* indicates decreases in the MRS parameter and VF total deviation (i.e., worse VF loss/positive correlation), and vice versa for *red*. *$P < 0.05$, **$P < 0.01$; ns, not significant.

TABLE 3. Optic Radiation Microstructural DTI Versus Archetypal VF Loss Patterns

		Normal Archetype	Positively Correlated Archetypes			Negatively Correlated Archetypes		
			1st	2nd	3rd	1st	2nd	3rd
Axial Diffusivity								
Right eye	Archetype no.	1	2	13	9	8	15	16
	Coefficients	112.90%	16.71%	11.44%	9.83%	−70.67%	−51.25%	−22.86%
	P	0.0652	0.3208	0.4207	0.0959	0.0535	0.0087	0.1813
Left eye	Archetype no.	1	6	11	10	13	5	2
	Coefficients	84.40%	13.70%	13.45%	12.56%	−47.13%	−31.64%	−14.12%
	P	0.1617	0.6978	0.1394	0.3345	0.0722	0.1647	0.48
Radial Diffusivity								
Right eye	Archetype no.	1	6	7	8	15	2	5
	Coefficients	−154.19%	105.87%	29.99%	22.73%	−19.04%	−11.65%	−8.12%
	P	0.0376	0.0404	0.0587	0.615	0.4355	0.5704	0.6493
Left eye	Archetype no.	1	6	11	8	2	5	4
	Coefficients	−145.64%	94.39%	39.50%	39.39%	−53.07%	−36.66%	−15.11%
	P	0.043	0.0232	0.0001	0.2736	0.0246	0.1815	0.211
Mean Diffusivity								
Right eye	Archetype no.	1	6	13	7	15	8	5
	Coefficients	−55.48%	80.47%	23.77%	20.74%	−44.72%	−23.22%	−16.92%
	P	0.4979	0.155	0.2029	0.2326	0.0883	0.636	0.3815
Left eye	Archetype no.	1	6	11	10	2	5	16
	Coefficients	−66.77%	82.58%	38.99%	32.28%	−50.12%	−47.18%	−9.05%
	P	0.4015	0.0707	0.0007	0.0559	0.0527	0.1135	0.5185
Fractional Anisotropy								
Right eye	Archetype no.	1	2	14	4	6	8	7
	Coefficients	425.55%	51.57%	17.01%	15.13%	−210.15%	−143.58%	−62.53%
	P	5.00E-04	0.1364	0.3821	0.2168	0.016	0.058	0.0194
Left eye	Archetype no.	1	2	5	4	6	13	8
	Coefficients	352.06%	92.08%	44.38%	40.90%	−153.17%	−118.13%	−101.26%
	P	0.0031	0.0207	0.3398	0.0426	0.0294	0.0256	0.0931

Linear mixed-effect analyses were performed to show how the DTI-VF models are associated with the 16 VF loss ATs. Coefficients for the normal archetype (AT1) and the top three most positively or negatively correlated VF loss ATs are presented. A positive coefficient for the AT1 indicates increasing DTI metrics with less VF loss, and vice versa; a positive coefficient for the other VF loss ATs indicates increasing DTI metrics with greater VF loss, and vice versa.

TABLE 4. Optic Radiation Microstructural DKI Versus Archetypal VF Loss Patterns

		Normal Archetype	Positively Correlated Archetypes			Negatively Correlated Archetypes		
			1st	2nd	3rd	1st	2nd	3rd
Axial Kurtosis								
Right eye	Archetype no.	1	16	5	2	6	8	3
	Coefficients	64.62%	60.94%	50.22%	29.92%	−137.40%	−60.02%	−48.52%
	P	0.6055	0.0753	0.0861	0.3784	0.1111	0.4222	0.2853
Left eye	Archetype no.	1	5	14	2	6	9	8
	Coefficients	79.02%	37.18%	35.42%	29.23%	−67.52%	−35.35%	−32.66%
	P	0.517	0.4216	0.152	0.3937	0.3445	0.2493	0.5915
Radial Kurtosis								
Right eye	Archetype no.	1	4	2	5	6	8	7
	Coefficients	140.27%	8.54%	5.84%	3.77%	−67.10%	−34.12%	−22.06%
	P	0.0002	0.0232	0.5922	0.6912	0.0136	0.1517	0.0078
Left eye	Archetype no.	1	2	4	14	6	13	8
	Coefficients	151.19%	24.12%	2.59%	1.79%	−44.30%	−24.64%	−23.21%
	P	0.0001	0.0251	0.6932	0.8223	0.0498	0.1504	0.2314
Mean Kurtosis								
Right eye	Archetype no.	1	15	5	10	6	7	3
	Coefficients	105.65%	32.75%	27.03%	16.71%	−107.75%	−34.03%	−26.88%
	P	0.2497	0.271	0.2128	0.4558	0.0896	0.0797	0.423
Left eye	Archetype no.	1	2	12	14	3	9	6
	Coefficients	156.22%	38.57%	14.71%	13.10%	−63.46%	−45.20%	−45.13%
	P	0.1241	0.1241	0.3222	0.4753	0.1486	0.0431	0.3917

Linear mixed-effect analyses were performed to show how the DKI-VF models are associated with the 16 VF loss ATs. Coefficients for the normal archetype (AT1) and the top three most positively or negatively correlated ATs are presented. A positive coefficient for the AT1 indicates increasing DKI metrics with less VF loss, and vice versa; a positive coefficient for the other VF loss ATs indicates increasing DKI metrics with greater VF loss, and vice versa.

TABLE 5. Optic Radiation Microstructural WMTI Versus Archetypal VF Loss Patterns

		Normal Archetype	Positively Correlated Archetypes			Negatively Correlated Archetypes		
			1st	2nd	3rd	1st	2nd	3rd
Intra-Axonal Space Axial Diffusivity								
Right eye	Archetype no.	1	2	4	14	8	6	15
	Coefficients	424.10%	47.23%	20.15%	14.07%	−198.69%	−128.63%	−91.68%
	P	0.0001	0.1175	0.0571	0.4073	0.002	0.0952	0.0093
Left eye	Archetype no.	1	2	4	10	13	6	3
	Coefficients	402.84%	60.20%	28.80%	12.45%	−110.66%	−108.24%	−94.25%
	P	0.00001	0.0465	0.1122	0.5997	0.019	0.0876	0.0758
Tortuosity of EAS								
Right eye	Archetype no.	1	2	14	4	6	8	7
	Coefficients	102.47%	16.84%	8.00%	3.18%	−53.83%	−37.81%	−12.02%
	P	0.0006	0.0437	0.0878	0.2856	0.0109	0.0394	0.0669
Left eye	Archetype no.	1	2	4	5	6	13	8
	Coefficients	80.38%	16.85%	11.55%	7.60%	−38.32%	−28.18%	−19.69%
	P	0.0064	0.0455	0.0206	0.5101	0.0286	0.0326	0.1916
EASD Parallel								
Right eye	Archetype no.	1	2	13	9	8	15	6
	Coefficients	154.67%	25.37%	11.25%	9.91%	−92.54%	−51.79%	−36.09%
	P	0.0066	0.1088	0.4026	0.0753	0.0066	0.0049	0.3763
Left eye	Archetype no.	1	10	11	2	13	5	3
	Coefficients	110.51%	17.83%	11.37%	6.38%	−62.37%	−24.00%	−15.19%
	P	0.0501	0.1488	0.1911	0.6925	0.0114	0.2678	0.59
EASD Perpendicular								
Right eye	Archetype no.	1	6	7	13	15	2	14
	Coefficients	−123.90%	87.11%	23.11%	18.50%	−17.36%	−11.27%	−8.72%
	P	0.0631	0.0605	0.1051	0.2302	0.4274	0.5399	0.395
Left eye	Archetype no.	1	6	10	8	5	2	3
	Coefficients	−117.90%	85.60%	36.49%	35.61%	−36.45%	−33.68%	−22.30%
	P	0.0701	0.0239	0.0088	0.277	0.1422	0.0658	0.4916
Axonal Water Fraction								
Right eye	Archetype no.	1	2	15	16	6	8	7
	Coefficients	443.49%	48.80%	44.55%	42.63%	−330.58%	−125.29%	−73.91%
	P	0.0415	0.4168	0.5342	0.4869	0.0287	0.343	0.1136
Left eye	Archetype no.	1	2	5	14	6	3	8
	Coefficients	543.38%	133.24%	53.52%	31.00%	−222.19%	−144.92%	−97.13%
	P	0.0096	0.0251	0.5134	0.4813	0.0758	0.1696	0.3658

Linear mixed-effect analyses were performed to show how the WMTI-VF models are associated with the 16 VF loss ATs. Coefficients for the normal archetype (AT1) and the top three most positively or negatively correlated VF loss ATs are presented. A positive coefficient for the AT1 indicates increasing WMTI metrics with less VF loss, and vice versa; a positive coefficient for the other VF loss ATs indicates increasing WMTI metrics with greater VF loss, and vice versa. EASD parallel represents axial EASD, and EASD perpendicular represents radial EASD. Tortuosity of EAS is the ratio of EASD parallel to EASD perpendicular.

glaucoma. MLP was able to differentiate between healthy control and early glaucoma (accuracy, 90.9%; ROC, 0.99) and between healthy control and advanced glaucoma (accuracy, 97.9%; ROC, 1.000).

DISCUSSION

This study found that, in diffusion MRI of the optic radiation, fractional anisotropy, radial diffusivity, radial kurtosis, axonal water fraction, tortuosity, and EASD perpendicular correlated with overall visual field loss in glaucoma patients. Regionally, decreasing intra-axonal space axial diffusivity in WMTI tended to associate with greater visual field loss in the superior–altitudinal area of the right eye and the inferior–altitudinal area of the left eye in a complementary pattern, as shown in both partial correlations (Fig. 2) and archetypal analyses (Table 5). Radial diffusivity, radial kurtosis, tortuosity, and EASD also tended to show complementary visual field loss patterns in the peripheral versus

central areas or in the superior versus inferior areas between the left and right eyes. In MRS of the visual cortex, lower GABA, glutamate, and choline levels were found in early and advanced glaucoma patients compared to healthy subjects. Complementary visual field loss patterns were also observed among neurometabolites, with GABA affecting the superonasal areas more and glutamate and choline affecting the inferior areas more. These advanced MRI/MRS imaging biomarkers not only allowed detection of microstructural and metabolic brain alterations associated with the visual field deficits in glaucoma but also highlighted their potential for understanding its pathogenesis and neuroadaptation to bilateral visual outcomes.

Diffusion MRI biomarkers, which are sensitive to axonal or glial integrity and neuroinflammation, not only correlated with overall visual field loss but also showed complementary archetypal patterns of regional visual field loss between the two eyes in glaucoma patients. The findings are consistent with previous studies showing that local loss of visual function in one eye is often spared in the same

TABLE 6. Visual Cortex Metabolism in Proton MRS Versus Archetypal VF Loss Patterns

		Normal Archetype	Positively Correlated Archetypes			Negatively Correlated Archetypes		
			1st	2nd	3rd	1st	2nd	3rd
GABA								
Right eye	Archetype no.	1	9	12	7	6	15	16
	Coefficients	227.22%	32.01%	11.93%	10.61%	−72.79%	−57.46%	−21.02%
	P	0.0039	0.0314	0.4167	0.0815	0.0521	0.0033	0.229
Left eye	Archetype no.	1	2	10	4	6	3	15
	Coefficients	135.82%	93.87%	30.03%	23.41%	−27.88%	−8.73%	−4.42%
	P	0.0119	0.0745	0.0647	0.189	0.0877	0.0786	0.6877
Glutamate								
Right eye	Archetype no.	1	7	8	12	6	2	15
	Coefficients	23.48%	0.1349	0.1294	0.0372	−1.3499	−0.6437	−0.1479
	P	0.651	0.2764	0.3078	0.304	0.0822	0.1183	0.2465
Left eye	Archetype no.	1	3	2	8	6	5	13
	Coefficients	34.56%	13.49%	12.94%	3.72%	−134.99%	−84.37%	−74.79%
	P	0.0324	0.0764	0.1078	0.0504	0.0422	0.1083	0.0665
Choline								
Right eye	Archetype no.	1	4	9	12	6	10	15
	Coefficients	152.90%	45.99%	32.84%	10.06%	−56.86%	−39.00%	−21.87%
	P	0.0251	0.0708	0.2887	0.5602	0.157	0.0304	0.1228
Left eye	Archetype no.	1	14	12	2	5	13	6
	Coefficients	124.19%	78.11%	40.95%	36.66%	−22.19%	−10.59%	−8.80%
	P	0.0143	0.0912	0.3018	0.0617	0.1708	0.3007	0.2177

Linear mixed-effect analyses were performed to show how the MRS-VF models are associated with the 16 VF loss ATs. Coefficients for the normal archetype (AT1) and the top three most positively or negatively correlated VF loss ATs are presented. A positive coefficient for the AT1 indicates increasing MRS metrics with less VF loss, and vice versa; a positive coefficient for the other VF loss ATs indicates increasing MRS metrics with greater VF loss, and vice versa.
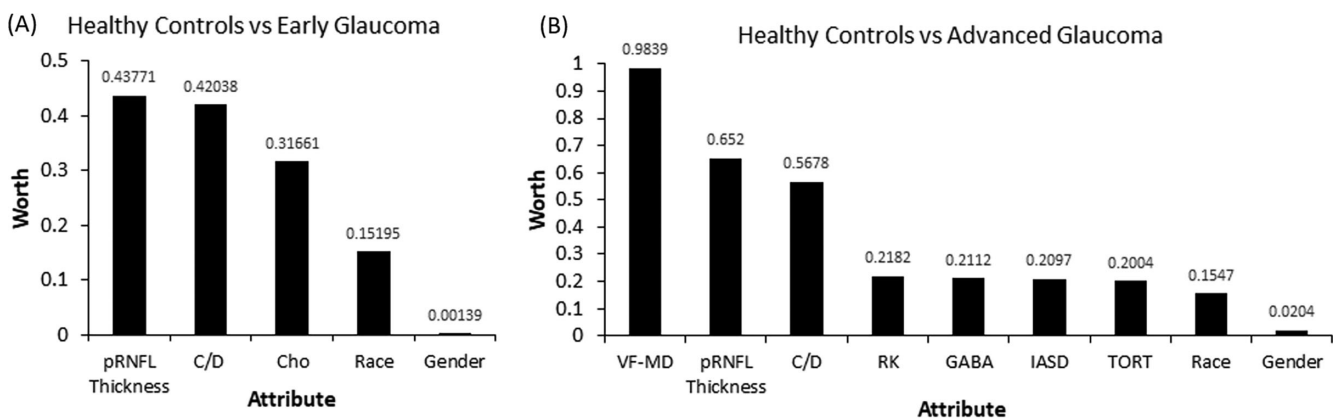

FIGURE 4. Visual display of ranked attributes in order of importance in early glaucoma (**A**) and advanced glaucoma (**B**) compared to healthy controls. Twenty-one attributes were fed into the InfoGain software, and the plotted attributes in **A** and **B** were deemed to have the greatest attribute worth in distinguishing between healthy controls and glaucoma in their respective stages. In **A**, the most important attributes when comparing healthy controls and early glaucoma patients, in descending order of attribute worth, were pRNFL thickness, cup-to-disc ratio (C/D), choline, race, and gender. In **B**, the most important attributes when comparing healthy controls and advanced glaucoma patients, in descending order of attribute worth, were VF-MD, pRNFL thickness, C/D, radial kurtosis (RK), GABA, intra-axonal space axial diffusivity (IASD), tortuosity (TORT), race, and gender.

visual field region of the contralateral eye, maximizing residual binocular visual function.[45–48] This suggests that alterations in the microstructural environment of the brain may contribute to the neuromodulation of preferential visual field loss patterns that help maximize residual binocular vision in bilateral glaucoma. The advanced diffusion MRI techniques, combined with archetypal analysis, provided unique insights into the potential role of microstructural changes in optimizing compensatory visual function when both eyes are affected by the disease.

There are several possible explanations for such complementary patterns. One such explanation is that the structural integrity of axons and glial cells, as measured by diffusion MRI, may be adapting in a compensatory way to optimize remaining binocular vision. For example, if certain axons projecting to a deteriorated part of the visual field in one eye are damaged, this could disinhibit the corresponding axons projecting to the same visual field region in the other eye.[45,47] Complementary visual field loss patterns could be an endpoint result of preferential

degeneration of visual pathways from each eye to optimize binocular vision. Another explanation is that complementary patterns of visual field loss and the associated microstructural changes detected by diffusion MRI may reflect adaptive or compensatory degeneration of visual pathways in response to disease progression, rather than being the direct underlying cause of the preferential regional deficits themselves.[70] Other factors affecting axonal health, glial cell integrity, inflammation, or selective vulnerability of visual pathways could also lead to emergent complementary patterns of visual field loss that are measurable with diffusion MRI.[21,49,50] This research highlights the significant impact that brain microstructural changes can have on overall visual function and symptoms in patients.[51–53] This underscores the importance of assessing imaging biomarkers contributions to vision loss in glaucoma.

The MRS neurometabolites, GABA, glutamate, and choline were found to relate to matching regional patterns of visual field loss in glaucoma patients. Specifically, GABA levels appeared to correlate more with vision loss in the superonasal areas of the visual field, and glutamate and choline levels correlated more with vision loss in the inferior areas of the visual field. GABA is the major inhibitory neurotransmitter in the brain,[54] and studies have shown that reduced GABA levels in the occipital cortex could lead to reduced inhibition and excessive excitatory activity,[55,56] which may contribute to visual field loss in glaucoma. Glutamate is the major excitatory neurotransmitter,[57] and choline is a marker of cell membrane integrity and neurotransmission, which interacts with GABA and glutamate.[5] The excitatory and inhibitory balance between these metabolites may also reflect neuroplastic potentials.[58] The regional visual field differences in these metabolites in the visual cortex may reflect such potential neuroadaptation. On the other hand, glutamate together with axial diffusivity tended to show opposite local visual field loss patterns between the two eyes in the superior peripheral area (AT2), with glutamate trending to associate negatively with worse AT2 in the right eye but positively in the left eye, whereas worse AT2 was trending to associate with decreasing axial diffusivity in the left eye but increasing axial diffusivity in the right eye. The complementary and opposite patterns within and between eyes across neurochemical and microstructural environments may be related to the redistribution of metabolic resources in the visual pathways and representations of the visual field in various parts of the brain.[59–61,70,71] More research is needed to clarify the precise mechanisms linking metabolic changes to complementary patterns of vision loss in glaucoma. In summary, these MRS spectral biomarkers may help determine the underlying disease mechanisms and neuroplasticity that occur in the brain in association with the characteristic regional patterns of visual field loss seen in both eyes of glaucoma patients. Determining these brain alterations related to the regional visual deficits in glaucoma could provide insight into the pathogenesis of the disease and the compensatory responses of the brain to the progressive vision loss.

The comparisons of healthy subjects to early and advanced glaucoma share several high-ranking attributes in terms of information gained, including pRNFL thickness, cup-to-disc ratio, race, and gender. Interestingly, the comparison of healthy subjects to early glaucoma uniquely showed choline as an important risk factor. Likewise, the comparison of healthy subjects to advanced glaucoma uniquely showed GABA and several DKI and WMTI measures as important

risk factors. Furthermore, we saw an improved ability of MLP to differentiate between healthy control and glaucoma when we only considered the attributes with an information gain worth >0, underscoring the importance of further research into these high-ranking attributes as risk factors for glaucoma. Overall, these results provide insight into the relationships among the eye, brain, and glaucoma, as well as the potential contribution of choline to early glaucoma and GABA and various diffusion MRI measures to advanced glaucoma.

The findings from this study highlight the potential of advanced MRI techniques, including diffusion MRI and MRS, as imaging biomarkers for tracking glaucoma detection, progression, and relevance to regional patterns of visual field loss. However, given its cross-sectional nature, causality cannot be derived from this observational evaluation. Further longitudinal studies are required to understand the pathophysiological events and to determine their utility for early detection and ongoing monitoring of disease severity with relevance to vision loss. The complementary archetypal patterns of visual field deficits between eyes when relating to the structural changes in the optic radiation or metabolic changes in the visual cortex suggest that the brain may be adapting to maximize remaining binocular vision, which merits further exploration of the plasticity mechanisms of the brain.[45] For example, future studies can employ high-resolution MRI/MRS for probing the precise brain changes, together with comprehensive whole-brain analyses to examine other brain regions that may be involved in abnormal visual processing and metabolic redistribution in glaucoma, such as the optic nerve, optic tract, lateral geniculate nucleus, superior colliculus, higher order visual brain areas, or other non–image-forming brain regions.[6,16,59,62–65] Another limitation is the relatively small sample size due to the strict recruiting conditions. Additional research on larger, more diverse patient samples from multiple centers is warranted to elucidate the structure–metabolism–function relationships between localized visual field loss and associated alterations in brain MRI metrics and metabolites. This could provide insight into disease pathogenesis and compensatory responses with improved generalizability. Other possible limitations lie in our assessments of visual function, as the Humphrey 24-2 visual field tests have been shown to miss central defects compared to 10-2 tests.[66] Future studies may consider the relationships between brain MRI/MRS metrics and central vision using 10-2 tests,[34,35,52] in addition to emerging methods such as microperimetry that allow for simultaneous fundus viewing with perimetry. Overall, advanced MRI techniques show promise as non-invasive biomarkers for understanding the brain contributions to characteristic visual field loss patterns in glaucoma. Further translational research could facilitate clinical implementation for improved glaucoma understanding and management.

References

1. Weinreb RN, Aung T, Medeiros FA. The pathophysiology and treatment of glaucoma: a review. *JAMA*. 2014;311:1901–1911.

2. Kapetanakis VV, Chan MP, Foster PJ, Cook DG, Owen CG, Rudnicka AR. Global variations and time trends in the prevalence of primary open angle glaucoma (POAG): a systematic review and meta-analysis. *Br J Ophthalmol*. 2016;100:86–93.

3. Tham YC, Li X, Wong TY, Quigley HA, Aung T, Cheng CY. Global prevalence of glaucoma and projections of glaucoma burden through 2040: a systematic review and meta-analysis. *Ophthalmology*. 2014;121:2081–2090.

4. Berdahl JP, Allingham RR. Intracranial pressure and glaucoma. *Curr Opin Ophthalmol*. 2010;21:106–111.

5. Faiq MA, Wollstein G, Schuman JS, Chan KC. Cholinergic nervous system and glaucoma: from basic science to clinical applications. *Prog Retin Eye Res*. 2019;72:100767.

6. Chan RW, Won Bang J, Trivedi V, et al. Relationships between cerebrovascular reactivity, visual-evoked functional activity, and resting-state functional connectivity in the visual cortex and basal forebrain in glaucoma. *Annu Int Conf IEEE Eng Med Biol Soc*. 2021;2021:4037–4040.

7. Faiq MA, Sengupta T, Nath M, et al. Ocular manifestations of central insulin resistance. *Neural Regen Res*. 2023;18:1139–1146.

8. Stein JD, Khawaja AP, Weizer JS. Glaucoma in adults—screening, diagnosis, and management: a review. *JAMA*. 2021;325:164–174.

9. Beykin G, Norcia AM, Srinivasan VJ, Dubra A, Goldberg JL. Discovery and clinical translation of novel glaucoma biomarkers. *Prog Retin Eye Res*. 2021;80:100875.

10. Ma D, Pasquale LR, Girard MJA, et al. Reverse translation of artificial intelligence in glaucoma: connecting basic science with clinical applications. *Front Ophthalmol (Lausanne)*. 2023;2:1057896.

11. Gupta N, Ang LC, Noel de Tilly L, Bidaisee L, Yucel YH. Human glaucoma and neural degeneration in intracranial optic nerve, lateral geniculate nucleus, and visual cortex. *Br J Ophthalmol*. 2006;90:674–678.

12. Gupta N, Greenberg G, de Tilly LN, Gray B, Polemidiotis M, Yucel YH. Atrophy of the lateral geniculate nucleus in human glaucoma detected by magnetic resonance imaging. *Br J Ophthalmol*. 2009;93:56–60.

13. Garaci FG, Bolacchi F, Cerulli A, et al. Optic nerve and optic radiation neurodegeneration in patients with glaucoma: in vivo analysis with 3-T diffusion-tensor MR imaging. *Radiology*. 2009;252:496–501.

14. Yucel YH, Gupta N. A framework to explore the visual brain in glaucoma with lessons from models and man. *Exp Eye Res*. 2015;141:171–178.

15. You Y, Joseph C, Wang C, et al. Demyelination precedes axonal loss in the transneuronal spread of human neurodegenerative disease. *Brain*. 2019;142:426–442.

16. Kasi A, Faiq MA, Chan KC. In vivo imaging of structural, metabolic and functional brain changes in glaucoma. *Neural Regen Res*. 2019;14:446–449.

17. Sun Z, Parra C, Bang JW, et al. Diffusion kurtosis imaging reveals optic tract damage that correlates with clinical severity in glaucoma. *Annu Int Conf IEEE Eng Med Biol Soc*. 2020;2020:1746–1749.

18. van der Merwe Y, Murphy MC, Sims JR, et al. Citicoline modulates glaucomatous neurodegeneration through intraocular pressure-independent control. *Neurotherapeutics*. 2021;18:1339–1359.

19. Zikou AK, Kitsos G, Tzarouchi LC, Astrakas L, Alexiou GA, Argyropoulou MI. Voxel-based morphometry and diffusion tensor imaging of the optic pathway in primary open-angle glaucoma: a preliminary study. *AJNR Am J Neuroradiol*. 2012;33:128–134.

20. Yang XL, van der Merwe Y, Sims J, et al. Age-related changes in eye, brain and visuomotor behavior in the DBA/2J mouse model of chronic glaucoma. *Sci Rep*. 2018;8:4643.

21. Mendoza M, Shotbolt M, Faiq MA, Parra C, Chan KC. Advanced diffusion MRI of the visual system in glaucoma: from experimental animal models to humans. *Biology (Basel)*. 2022;11:454.

22. Colbert MK, Ho LC, van der Merwe Y, et al. Diffusion tensor imaging of visual pathway abnormalities in five glaucoma animal models. *Invest Ophthalmol Vis Sci*. 2021;62:21.

23. Kruper J, Richie-Halford A, Benson N, et al. Convolutional neural network-based classification of glaucoma using optic radiation tissue properties. *Commun Med*. 2024;4(1):72.

24. Aksoy DO, Umurhan Akkan JC, Alkan A, Aralasmak A, Otcu Temur H, Yurtsever I. Magnetic resonance spectroscopy features of the visual pathways in patients with glaucoma. *Clin Neuroradiol*. 2019;29:615–621.

25. Bang JW, Parra C, Yu K, Wollstein G, Schuman JS, Chan KC. GABA decrease is associated with degraded neural specificity in the visual cortex of glaucoma patients. *Commun Biol*. 2023;6:679.

26. Yucel Y, Gupta N. Glaucoma of the brain: a disease model for the study of transsynaptic neural degeneration. *Prog Brain Res*. 2008;173:465–478.

27. Burgansky-Eliash Z, Wollstein G, Chu T, et al. Optical coherence tomography machine learning classifiers for glaucoma detection: a preliminary study. *Invest Ophthalmol Vis Sci*. 2005;46:4147–4152.

28. Um TW, Sung KR, Wollstein G, Yun SC, Na JH, Schuman JS. Asymmetry in hemifield macular thickness as an early indicator of glaucomatous change. *Invest Ophthalmol Vis Sci*. 2012;53:1139–1144.

29. Cutler A, Breiman L. Archetypal analysis. *Technometrics*. 1994;36:338–347.

30. Elze T, Pasquale LR, Shen LQ, Chen TC, Wiggs JL, Bex PJ. Patterns of functional vision loss in glaucoma determined with archetypal analysis. *J R Soc Interface*. 2015;12:20141118.

31. Keltner JL, Johnson CA, Cello KE, et al. Classification of visual field abnormalities in the ocular hypertension treatment study. *Arch Ophthalmol*. 2003;121:643–650.

32. Wang M, Pasquale LR, Shen LQ, et al. Reversal of glaucoma hemifield test results and visual field features in glaucoma. *Ophthalmology*. 2018;125:352–360.

33. Wang M, Shen LQ, Pasquale LR, et al. An artificial intelligence approach to detect visual field progression in glaucoma based on spatial pattern analysis. *Invest Ophthalmol Vis Sci*. 2019;60:365–375.

34. Wang M, Shen LQ, Pasquale LR, et al. Artificial intelligence classification of central visual field patterns in glaucoma. *Ophthalmology*. 2020;127:731–738.

35. Wang M, Tichelaar J, Pasquale LR, et al. Characterization of central visual field loss in end-stage glaucoma by unsupervised artificial intelligence. *JAMA Ophthalmol*. 2020;138:190–198.

36. Ades-Aron B, Veraart J, Kochunov P, et al. Evaluation of the accuracy and precision of the diffusion parameter EStImation with Gibbs and NoisE removal pipeline. *NeuroImage*. 2018;183:532–543.

37. Fieremans E, Jensen JH, Helpern JA. White matter characterization with diffusional kurtosis imaging. *NeuroImage*. 2011;58:177–188.

38. Provencher SW. Automatic quantitation of localized in vivo ^{1}H spectra with LCModel. *NMR Biomed*. 2001;14:260–264.

39. Provencher SW. Estimation of metabolite concentrations from localized in vivo proton NMR spectra. *Magn Reson Med*. 1993;30:672–679.

40. Kouznetsova VL, Li J, Romm E, Tsigelny IF. Finding distinctions between oral cancer and periodontitis using saliva metabolites and machine learning. *Oral Dis*. 2021;27:484–493.

41. Tran V, Saad T, Tesfaye M, et al. *Helicobacter pylori* (*H. pylori*) risk factor analysis and prevalence prediction: a machine learning-based approach. *BMC Infect Dis*. 2022;22:655.

42. Asaduzzaman S, Masud FA, Bhuiyan T, Ahmed K, Paul BK, Rahman SAMM. Dataset on significant risk factors for Type 1 diabetes: a Bangladeshi perspective. *Data Brief*. 2018;21:700–708.

43. Dritsas E, Trigka M. Efficient data-driven machine learning models for cardiovascular diseases risk prediction. *Sensors (Basel)*. 2023;23:1161

44. Frank E, Hall MA, Witten IH. *The WEKA Workbench. Online Appendix for "Data Mining: Practical Machine Learning Tools and Techniques,"* 4th ed. Burlington, MA: Morgan Kaufmann; 2016:4.

45. Hoste AM. New insights into the subjective perception of visual field defects. *Bull Soc Belge Ophtalmol*. 2003;287:65–71.

46. Sponsel WE, Groth SL, Satsangi N, Maddess T, Reilly MA. Refined data analysis provides clinical evidence for central nervous system control of chronic glaucomatous neurodegeneration. *Transl Vis Sci Technol*. 2014;3:1.

47. Reilly MA, Villarreal A, Maddess T, Sponsel WE. Refined frequency doubling perimetry analysis reaffirms central nervous system control of chronic glaucomatous neurodegeneration. *Transl Vis Sci Technol*. 2015;4:7.

48. Sponsel WE, Johnson SL, Trevino R, et al. Pattern electroretinography and visual evoked potentials provide clinical evidence of CNS modulation of high- and low-contrast VEP latency in glaucoma. *Transl Vis Sci Technol*. 2017; 6:6.

49. Kim US, Mahroo OA, Mollon JD, Yu-Wai-Man P. Retinal ganglion cells-diversity of cell types and clinical relevance. *Front Neurol*. 2021;12:661938.

50. Fieremans E, Benitez A, Jensen JH, et al. Novel white matter tract integrity metrics sensitive to Alzheimer disease progression. *AJNR Am J Neuroradiol*. 2013;34:2105–2112.

51. Boucard CC, Hernowo AT, Maguire RP, et al. Changes in cortical grey matter density associated with long-standing retinal visual field defects. *Brain*. 2009;132:1898–1906.

52. Murphy MC, Conner IP, Teng CY, et al. Retinal structures and visual cortex activity are impaired prior to clinical vision loss in glaucoma. *Sci Rep*. 2016;6:31464.

53. Trivedi V, Bang JW, Parra C, et al. Widespread brain reorganization perturbs visuomotor coordination in early glaucoma. *Sci Rep*. 2019;9:14168.

54. Stagg CJ, Bachtiar V, Johansen-Berg H. What are we measuring with GABA magnetic resonance spectroscopy? *Commun Integr Biol*. 2011;4:573–575.

55. Henriksen S, Tanabe S, Cumming B. Disparity processing in primary visual cortex. *Philos Trans R Soc Lond B Biol Sci*. 2016;371:20150255.

56. Saionz EL, Busza A, Huxlin KR. Rehabilitation of visual perception in cortical blindness. *Handb Clin Neurol*. 2022;184:357–373.

57. Duncan JS. Magnetic resonance spectroscopy. *Epilepsia*. 1996;37:598–605.

58. Bang JW, Hamilton-Fletcher G, Chan KC. Visual plasticity in adulthood: perspectives from Hebbian and homeostatic plasticity. *Neuroscientist*. 2023;29:117–138.

59. Cooper ML, Pasini S, Lambert WS, et al. Redistribution of metabolic resources through astrocyte networks mitigates neurodegenerative stress. *Proc Natl Acad Sci USA*. 2020;117:18810–18821.

60. Lucas-Ruiz F, Galindo-Romero C, Albaladejo-Garcia V, Vidal-Sanz M, Agudo-Barriuso M. Mechanisms implicated in the contralateral effect in the central nervous system after unilateral injury: focus on the visual system. *Neural Regen Res*. 2021;16:2125–2131.

61. Zhou W, Muir ER, Nagi KS, Chalfin S, Rodriguez P, Duong TQ. Retinotopic fMRI reveals visual dysfunction and functional reorganization in the visual cortex of mild to moderate glaucoma patients. *J Glaucoma*. 2017;26:430–437.

62. DeCarlo AA, Hammes N, Johnson PL, Shekhar A, Samuels BC. Dual orexin receptor antagonist attenuates increases in IOP, ICP, and translaminar pressure difference after stimulation of the hypothalamus in rats. *Invest Ophthalmol Vis Sci*. 2022;63:1.

63. Massi L, Bang JW, Parra C, et al. Altered functional connectivity of the habenula and its implications in anxiety and visual cognition in glaucoma. *Invest Ophthalmol Vis Sci*. 2023;64:3262.

64. Bang JW, Parra C, Wollstein G, Schuman JS, Chan KC. Sleep-regulating systems are impaired in glaucoma. *Invest Ophthalmol Vis Sci*. 2021;62:2347.

65. Gonzalez Fleitas MF, Devouassoux J, Aranda ML, et al. Melatonin prevents non-image-forming visual system alterations induced by experimental glaucoma in rats. *Mol Neurobiol*. 2021;58:3653–3664.

66. De Moraes CG, Hood DC, Thenappan A, et al. 24-2 visual fields miss central defects shown on 10-2 tests in glaucoma suspects, ocular hypertensives, and early glaucoma. *Ophthalmology*. 2017;124:1449–1456.

67. Bou Ghanem GO, Wareham LK, Calkins DJ. Addressing neurodegeneration in glaucoma: mechanisms, challenges, and treatments. *Prog Retin Eye Res*. 2024;100:101261.

68. Wareham LK, Liddelow SA, Temple S, et al. Solving neurodegeneration: common mechanisms and strategies for new treatments. *Mol Neurodegener*. 2022;17(1):23.

69. Ma D, Deng W, Khera Z. Early inner plexiform layer thinning and retinal nerve fiber layer thickening in excitotoxic retinal injury using deep learning-assisted optical coherence tomography. *Acta Neuropathol Commun*. 2024;12(1):19.

70. Carvalho J, Invernizzi A, Martins J, et al. Local neuroplasticity in adult glaucomatous visual cortex. *Sci Rep*. 2022;12(1):21981.

71. González-Riquelme MJ, Caridad Galindo-Romero C, Fernando Lucas-RuizAxonal F, et al. Injuries cast long shadows: long term glial activation in injured and contralateral retinas after unilateral axotomy. *Int J Mol Sci*. 2021;22(16):8517.